

High-Efficiency Metasurface-Based Surface-Plasmon Lenses

Feifei Liu, Dongyi Wang, Han Zhu, Xiyue Zhang, Tong Liu, Shulin Sun, Xinping Zhang, Qiong He, and Lei Zhou*

A device that can couple propagating light into surface plasmon polaritons (SPPs) focused into a small region is highly desired for on-chip photonics applications (e.g., energy-harvesting, sensing, etc.). However, current technologies suffer from large device footprint, low working efficiency, and insufficient light-manipulation freedom. Here, a generic approach for designing plasmonic lenses to generate predesigned vector SPP vortices with high efficiencies is established. Constructed with a set of meta-atoms exhibiting tailored reflection phases and polarization-conversion capabilities, the devices can convert normally incident circularly polarized light into predesigned vector SPP vortices with high efficiencies, due to both phase and polarization matching. As the illustrations, this study experimentally demonstrates directional SPP conversion (coupling efficiency: 35%; utilization efficiency: 98%) and SPP focusing effect at the wavelength of 1064 nm, with two meta-couplers in stripe and arc shapes, respectively. Finally, a ring-shaped meta-coupler is designed/fabricated, and the generation of a vector SPP vortex with significantly enhanced efficiency as compared to previous schemes is experimentally demonstrated. The results pave the way for realizing on-chip plasmonic devices to efficiently utilize SPPs with minimal footprints.

1. Introduction

Surface plasmon polaritons (SPPs), surface electromagnetic (EM) eigen-modes coupled with collective oscillation of electrons at certain metal/dielectric interfaces,^[1] have attracted considerable research interests due to their capabilities of local field enhancement and subwavelength confinement.^[2–4] To efficiently utilize SPPs in on-chip photonics applications, various SPP-related devices are needed, including SPP couplers,^[5–7] plasmon waveguides,^[8–10] SPP lenses,^[11–14] and many others.

Among these devices, a plasmonic lens that can couple propagating light into near-field SPP patterns exhibiting predesigned properties has attracted considerable interests recently. For example, focusing cylindrically polarized SPPs into a small region can generate a tightly focused hotspot being highly desired for energy-harvesting,^[15,16] while creating

a SPP vortex carrying an optical angular momentum (OAM) can find interesting applications in nanoparticle trapping,^[17] rotating,^[18] super-resolution imaging, and data storage.^[19,20] To realize such plasmonic devices, a typical approach is to dip on metallic thin films various nanoholes or nanoslits, which are arranged in certain configurations (e.g., rings, spirals, etc.).^[21–28] The working principle of these meta-devices can be described as follows: a nanohole or a nanoslit serves as local coupler to convert free-space circularly polarized (CP) light into SPP with phase dictated by its orientation angle due to the Pancharatnam–Berry (PB) mechanism,^[29] while the interferences among these SPP waves form the final SPP wave-front as desired. Unfortunately, while nontrivial SPP patterns (including the vector SPP vortices) were indeed successfully generated based on such a scheme,^[30–32] the proposed devices are usually of very low working efficiencies, being unfavorable for practical applications. The inherent reason is that a nanohole (or nanoslit) can only convert a very small portion of free-space light into SPP (see **Figure 1a**), while a large portion of incident light has been reflected back leading to significant energy waste.

Metasurfaces, ultrathin metamaterials composed by subwavelength nanostructures exhibiting tailored optical properties, have attracted intensive interests due to their unrepresented capabilities to manipulate light in terms of wave-front and polarization.^[33–43] Recently, based on the metasurface concept, various plasmonic meta-devices were experimentally demonstrated in the terahertz

F. Liu

College Physics and Materials Science
Tianjin Normal University
Tianjin 300387, P. R. China


F. Liu, D. Wang, H. Zhu, X. Zhang, T. Liu, Q. He, L. Zhou
State Key Laboratory of Surface Physics and Department of Physics
Fudan University
Shanghai 200433, P. R. China
E-mail: phzhou@fudan.edu.cn

S. Sun

Shanghai Engineering Research Centre of Ultra Precision Optical
Manufacturing
Department of Optical Science and Engineering
School of Information Science and Technology
Fudan University
Shanghai 200433, P. R. China

X. Zhang

Institute of Information Photonics Technology and College of Applied
Sciences
Beijing University of Technology
Beijing 100124, P. R. China

 The ORCID identification number(s) for the author(s) of this article can be found under <https://doi.org/10.1002/lpor.202201001>

DOI: 10.1002/lpor.202201001

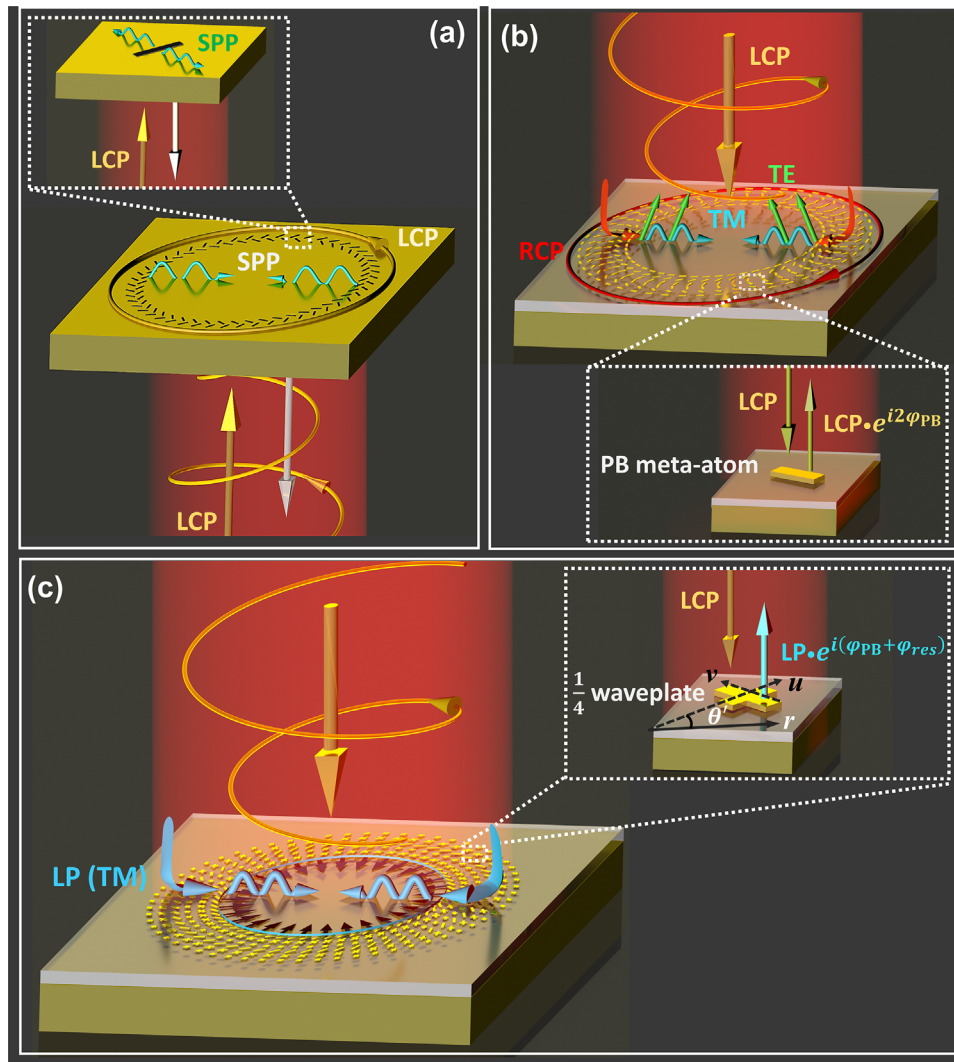


Figure 1. Schematics and working principle of the high-efficiency metasurface-based SPP lens. Schematics of the SPP lenses constructed by a) nanoslits, b) PB meta-atoms exhibiting 100%-efficiency PCR, and c) our meta-atoms exhibiting desired reflection phases and polarization-conversion abilities, respectively. Insets in different subfigures schematically depict the corresponding meta-atoms and their wave-scattering properties.

(THz) regime, which can first convert free-space THz waves into SPPs and then manipulate the wave-front of the generated SPP beams. Such meta-devices are composed by meta-atoms exhibiting tailored reflection phases for incident CP THz light, dictated by both resonance mechanism and the PB one,^[5,36,44,45] so that the whole devices can encode certain phase profiles to enable both SPP conversion and wave-front manipulation. Compared to nano-hole-based plasmonic devices, these meta-devices possess much higher working efficiencies, since the adopted meta-atoms can be purposely designed to exhibit high polarization-conversion ratios (PCRs) as requested by the PB mechanism (see inset in Figure 1b).^[46] Unfortunately, so far plasmonic meta-lenses based on this scheme have not been realized at optical frequencies. Also, devices designed with this scheme cannot generate vector SPPs, since waves scattered by different meta-atoms all exhibit the same circular polarizations. Finally, polarization mismatch between circular polarization of scattered waves and linear

polarization of SPP can cause reflections in the coupling process, inevitably deteriorating the coupling efficiency (see Figure 1b).^[47]

In this work, we propose an alternative strategy for designing plasmonic meta-lenses to generate arbitrary SPPs near-field patterns with high efficiencies. Composed by a series of meta-atoms with predesigned reflection phases and polarization-conversion capabilities, our plasmonic lens can efficiently convert a normally incident CP light to a cylindrically polarized SPP exhibiting a desired wave-front due to both momentum and polarization match (see Figure 1c). After designing a series of meta-atoms with desired optical properties, we perform a benchmark experiment to characterize the SPP coupling efficiency of a stripe-shape coupler constructed by these meta-atoms. We next fabricate two plasmonic lenses, with the designed meta-atoms arranged in arc or ring shapes, respectively, and experimentally characterize their functionalities. Our experiments clearly demonstrate that the first device can focus SPP to a single point, while the second

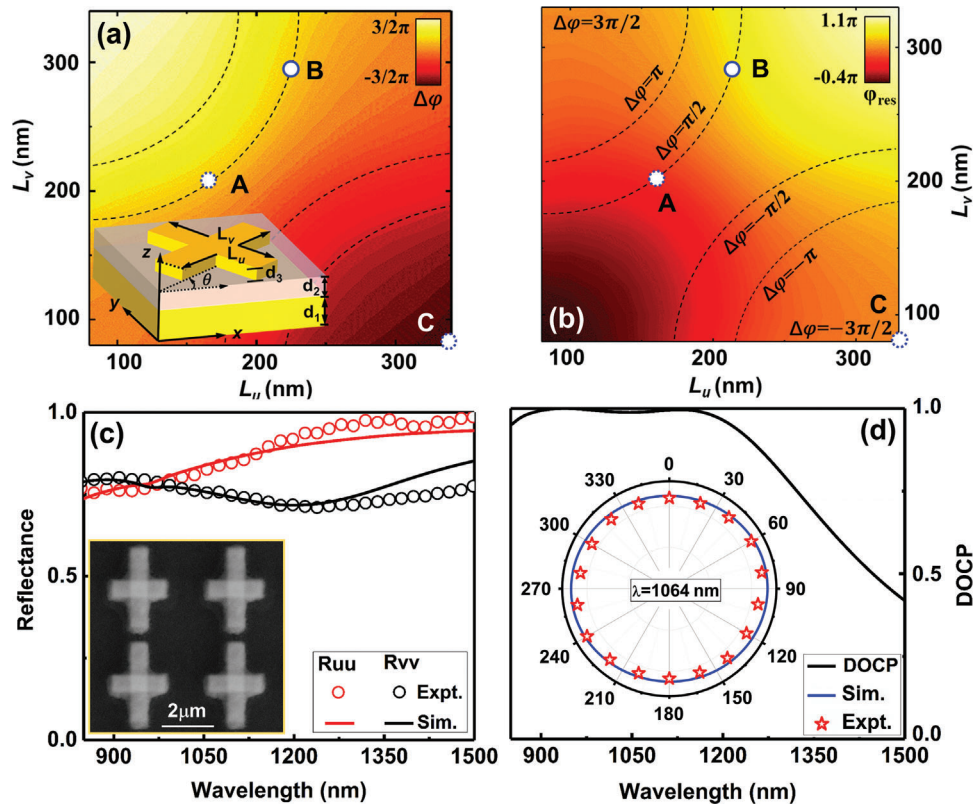


Figure 2. Design and characterization of meta-atoms. FDTD-computed a) $\Delta\phi$ and b) ϕ_{res} of MIM meta-atoms [see inset in (a) for geometry] with different L_u and L_v , arranged in square lattices with periodicity 310 nm. Here, other geometric parameters are fixed as $d_1 = 150\text{ nm}$, $d_2 = 100\text{ nm}$, $d_3 = 30\text{ nm}$. c) Measured (circles dotted curves) and simulated (solid curves) reflectance spectra of a metasurface containing meta-atoms “B” arranged in a square lattice with periodicity $P = 310\text{ nm}$, under normally incident light polarized along u and v axes, respectively. Inset depicts part of SEM image of the fabricated metasurface. d) Black line depicts the numerically calculated DOCP spectrum of the metasurface, with inset showing measured (red stars) and simulated (solid blue curve) polarized field patterns of light reflected by the metasurface shined by normally incident light with \mathbf{E} field lying at 45 degrees with respect to the u axis at the wavelength $\lambda = 1064\text{ nm}$.

device can form a standing-wave SPP pattern exhibiting strongly enhanced local-field and clear feature of OAM. Analytical calculations are in excellent agreement with both experimental and simulation results. Comparisons with previously achieved lenses show that the SPP hotspot realized by our device exhibits a much higher intensity (≈ 50 and 5 times higher than nanoslit meta-coupler and PB meta-coupler, respectively), which is better suited for on-chip photonic applications.

2. Results

2.1. Design and Characterization of the Meta-Atoms

Following the discussions in the Introduction (see Figure 1a,b), we understand that an ideal plasmonic meta-lens should be a carefully designed metasurface, which, under the illumination of a CP light, can generate a driven surface wave (SW) with \mathbf{k} vector and polarization matching those of the eigen SPP supported by the target plasmonic metal (see Figure 1c). Therefore, such a metasurface must exhibit a reflection-phase profile φ^o containing a gradient term $-\zeta r$ for the incident CP light with spin σ [$\sigma = 1$: left circular polarization (LCP), $\sigma = -1$: right circular polarization (RCP)], where the phase gradient is $\zeta = k_{spp} > k_0$ with k_{spp}

and k_0 being the wave-vectors of eigen SPP and free-space light, respectively. Also, the metasurface should be able to convert incident circular polarization to linear polarizations with \mathbf{E} field pointing along the pre-designed local directions. Therefore, we need to design a series of meta-atoms that can not only offer the desired reflection phases, but also behave as ideal quarter wave-plates.

We choose the working wavelength as $\lambda = 1064\text{ nm}$ to design a series of meta-atoms meeting the above requirements, and experimentally characterize their reflection properties. Inset to Figure 2a schematically depicts the geometry of the basic meta-atom that we choose, which is composed of a cross-shaped gold (Au) nanoantenna and a continuous Au film separated by a silica (SiO_2) spacer. The lengths of the nano-cross are L_u and L_v , with u and v denoting two principle axes, respectively, while the cross is rotated by an angle of θ against z -axis in laboratory (x - y) coordinate system. Thus, L_u , L_v , and θ are three parameters to dictate the reflection properties of a meta-atom, based on the relations that we derived below.

Suppose that a meta-atom exhibits the following reflection Jones' matrix $\mathbf{R}(0) = \begin{pmatrix} |r_{uu}|e^{i\varphi_u} & 0 \\ 0 & |r_{vv}|e^{i\varphi_v} \end{pmatrix}$ in linear-polarization bases and in local u - v coordinate system, with φ_u and φ_v

being the reflection phases for polarizations along two principle axes, respectively. Consider the ideal lossless case (i.e., $|r_{uu}| = |r_{vv}| = 1$) for the moment, the reflection Jones' matrix in laboratory coordinate system and in circular-polarization bases is then derived as $\tilde{\mathbf{R}}(\theta) = \mathbf{SM}(\theta)\mathbf{R}(0)\mathbf{M}^{-1}(\theta)\mathbf{S}^{-1} = \begin{pmatrix} e^{i\varphi_u} + e^{i\varphi_v} & e^{-i2\theta}(e^{i\varphi_u} - e^{i\varphi_v}) \\ e^{i2\theta}(e^{i\varphi_u} - e^{i\varphi_v}) & e^{i\varphi_u} + e^{i\varphi_v} \end{pmatrix}$, where $\mathbf{S} = \frac{\sqrt{2}}{2} \begin{pmatrix} 1 & -i \\ 1 & i \end{pmatrix}$ and $\mathbf{M}(\theta) = \begin{pmatrix} \cos(\theta) & -\sin(\theta) \\ \sin(\theta) & \cos(\theta) \end{pmatrix}$. Assuming that the incident light is a CP wave with spin σ , the reflected wave is calculated as

$$|\Psi_{\text{ref}}\rangle = \tilde{\mathbf{R}}(\theta) |\Psi_{\text{in}}\rangle = e^{i(\varphi_{\text{res}} + \sigma\theta)} \begin{pmatrix} e^{-i(\theta - \sigma \cdot \frac{\pi}{4})} \cos\left(\frac{\Delta\varphi}{2}\right) \\ e^{i(\theta - \sigma \cdot \frac{\pi}{4})} \sin\left(\frac{\Delta\varphi}{2}\right) \end{pmatrix} \quad (1)$$

with $\varphi_{\text{res}} = \frac{\varphi_u + \varphi_v}{2} - \frac{\pi}{4}$ and $\Delta\varphi = \varphi_v - \varphi_u$, dictated by the resonances and anisotropy of the meta-atom, respectively. Clearly, the reflected wave is generally elliptically polarized with ellipticity and polarization angle determined by $\Delta\varphi$ and $(\theta - \sigma \cdot \frac{\pi}{4})$, respectively. In the special case of $\Delta\varphi = \pi/2$ (i.e., the meta-atom is an ideal quarter wave-plate), we find that the reflected wave becomes

$$|\Psi_{\text{ref}}\rangle = e^{i(\varphi_{\text{res}} + \sigma\theta)} \begin{pmatrix} e^{-i(\theta - \sigma \cdot \frac{\pi}{4})} \\ e^{i(\theta - \sigma \cdot \frac{\pi}{4})} \end{pmatrix} = e^{i(\varphi_{\text{res}} + \sigma\theta)} \left[\cos\left(\theta - \sigma \cdot \frac{\pi}{4}\right) \hat{x} + \sin\left(\theta - \sigma \cdot \frac{\pi}{4}\right) \hat{y} \right]. \quad (2)$$

Equation (2) clearly shows that the reflected wave is linearly polarized along the direction determined by $(\theta - \sigma \cdot \frac{\pi}{4})$, with an additional phase $(\varphi_{\text{res}} + \sigma \cdot \theta)$ dictated by geometry (i.e., L_u and L_v) and orientation angle θ of the meta-atom.

We proceed to design a series of meta-atoms, all behaving as ideal quarter wave-plates ($\Delta\varphi = \pi/2$) but exhibiting different resonant phases φ_{res} . We first employ finite-difference time-domain (FDTD) simulations to study how $\Delta\varphi$ and φ_{res} of our meta-atoms vary against two geometric parameters (L_u and L_v) at the working wavelength 1064 nm, and depict them in two phase diagrams (Figure 2a,b). In our FDTD simulations, the top-most nano-crosses (with thickness $d_3 = 30$ nm) are repeatedly arranged in a square lattice with periodicity $P = 310$ nm and the bottom Au substrate has a thickness of $d_1 = 150$ nm. Since the thickness of SiO_2 layer can influence both the absorption and the magnetic resonant properties of our metal-insulator-metal (MIM) meta-atoms, it is an important parameter to determine the resonant phase φ_{res} coverage of our meta-atoms and the working efficiency of the whole device. After careful optimizations, we set the thickness of SiO_2 layer as $d_2 = 100$ nm in order to achieve a high working efficiency and a good performance for our meta-device. We successfully identify two meta-atoms from the $\Delta\varphi = \pi/2$ line in the phase diagram Figure 2a and mark them as blue circles labeled as "A" and "B". However, it is difficult for us to find the third meta-atom with appropriate phase differences with meta-atoms A and B on the $\Delta\varphi = \pi/2$ line. Alternatively, we find that the meta-atom with $L_u = 340$ nm and $L_v = 80$ nm has a value of $\Delta\varphi$ very close to $-\pi/2$ and a phase φ_{res} satisfying our requirements, which is thus chosen as our meta-atom "C" (see

Figure 2a). All these meta-atoms all have high reflectance and possess resonant phases $\varphi_{\text{res}} = 0.07\pi$, 0.68686π , and 1.36271π , respectively, which exhibit nearly equal phase steps covering the whole 2π range (see Figure 2b).

We experimentally characterize the optical properties of one of these meta-atoms (meta-atom "B"). We use standard electron-beam-lithography technique to fabricate out a metasurface sample containing meta-atoms with $L_u = 220$ nm and $L_v = 294$ nm arranged in a square lattice with periodicity $P = 310$ nm. Inset to Figure 2c depicts the scanning electron microscopic (SEM) image of part of the fabricated sample. Circles in Figure 2c represent the measured reflectance spectra of the sample under the illuminations of normally incident lights polarized along u and v directions, respectively, which are in nice agreement with corresponding FDTD simulations (solid curves). Two shallow dips appear at 850 and 1220 nm in two spectra, respectively, corresponding to two magnetic resonant modes for two orthogonal polarizations. Tuning L_u and L_v can efficiently change the resonant frequencies of these two magnetic modes, which can vary the values of φ_u and φ_v at the working wavelength (see Figure S1, Supporting Information), and in turn, modulate both $\Delta\varphi$ and φ_{res} dramatically. We note that the reflection amplitudes r_{uu} and r_{vv} are close to 80% at the working wavelength. While they are not 100% due to the absorption loss, the fact that $r_{uu} \approx r_{vv}$ ensures that Equations (1) and (2) are still valid. Unfortunately, our experimental setup is unable to characterize the reflection phases of the meta-atom directly. Instead, we can indirectly retrieve the information on $\Delta\varphi$ through experimentally characterizing the polarization state of light reflected by the metasurface at the working wavelength. In our experiment, we illuminate the sample by a linearly polarized light with E-field orientated at an angle 45° to the x-axis, and then measure the intensity of the reflected light passing through a rotatable linear polarizer placed in front of the sample. Inset to Figure 2d compares the measured and simulated field patterns of the reflected light passing through the polarizer tiled at different angles, which are in nice agreement with each other. A nearly circular pattern obtained in experiment clearly verifies that the meta-atom indeed behaves as a quarter wave-plate. To quantitatively characterize the performance of the meta-polarizer, we also calculate the degree of circular polarization (DOCP) of the reflected wave, using the formula $\text{DOCP} = |r_l^2 - r_r^2| / (r_l^2 + r_r^2)$ with r_l and r_r being the FDTD-simulated coefficients of LCP and RCP components inside the reflected beam. As shown in Figure 2d, DOCP of the reflected light exhibits broadband feature near the central wavelength, and reaches 99% with an absolute reflection efficiency 75% at $\lambda = 1064$ nm.

2.2. A Stripe-Shape Coupler: Unidirectional Excitation of SPP

We employ these meta-atoms to construct a stripe-shape meta-coupler and experimentally demonstrate the efficient unidirectional and polarization-selective excitation of SPP. Inset to Figure 3a schematically displays a supercell of the designed meta-coupler containing meta-atoms "A", "B" and "C", respectively. Meanwhile, the "plasmonic metal" is the same as the bottom structure of the meta-atom (i.e., an Au film covered by a silica spacer), in order to minimize light scatterings at the boundary between coupler and "plasmonic metal." To facilitate experimental

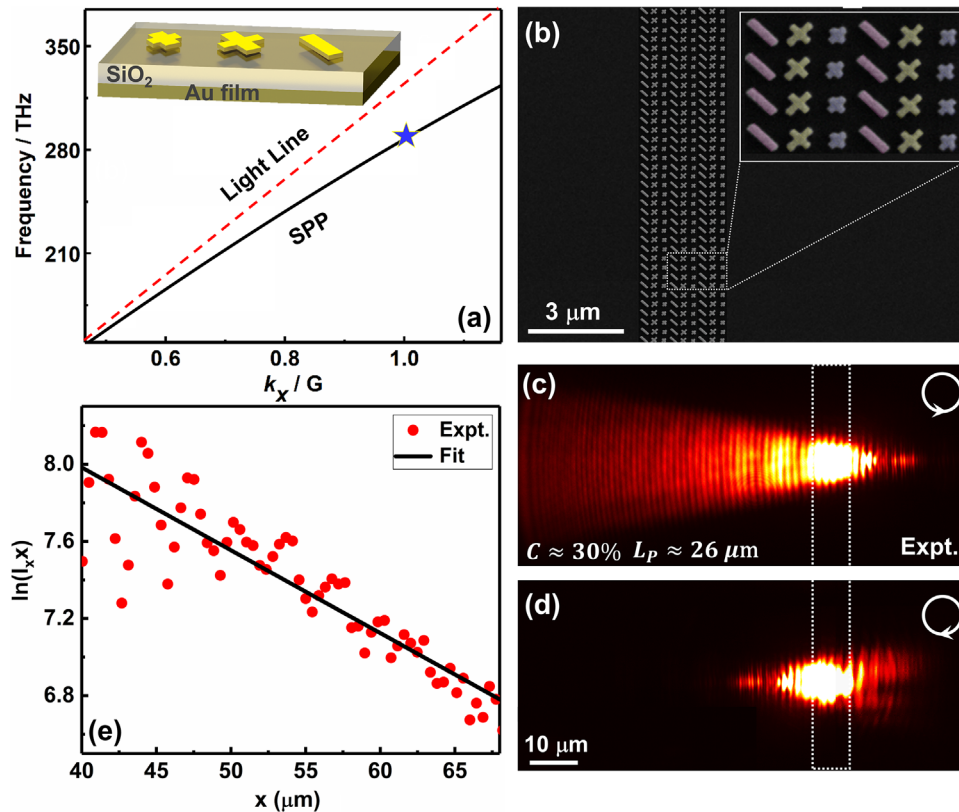


Figure 3. Design and characterization of the high-efficiency stripe-shaped SPP coupler. a) Dispersion relation of SPP mode supported by the guiding-out plasmonic metal with blue star representing the mode at 1064 nm; Inset shows the schematics of a super-cell of the designed stripe-shaped SPP coupler. b) SEM image of our fabricated sample containing the stripe-shaped SPP coupler and the guiding-out plasmonic metal. Inset shows a zoomed-in picture of the area surrounded by dotted lines. Geometric parameters of three meta-atoms: “A”, $L_u = 156$ nm, $L_v = 204$ nm, “B”, $L_u = 220$ nm, $L_v = 294$ nm, and “C”, $L_u = 334$ nm, $L_v = 80$ nm. c,d) LRM images of SPP generated on the surface of our sample which is shined by normally incident light at $\lambda = 1064$ nm with LCP and RCP, respectively. Areas surrounded by white dotted lines represent the positions of the meta-coupler. e) Measured $\ln(I_x)$ versus x (red circles), fitted by a straight line (solid line) with slope determining the propagation length of SPP.

characterizations on SPP using our leakage radiation microscopy (LRM), we purposely set the thickness of continuous Au film (in both all meta-atoms and the “plasmonic metal”) to 50 nm so that the generated SPP can be easily observed by the LRM. We note that shrinking the thickness of Au film from 150 to 50 nm does not significantly change the reflection phases of the adopted meta-atoms (see Figure S2, Supporting Information, for simulated results). Figure 3a depicts the analytically calculated dispersion of eigen SPP modes supported by such a “plasmonic metal,” showing that $k_{\text{SPP}} = 1.15 * 2\pi/\lambda$ at the working wavelength $\lambda = 1064$ nm as marked by blue star, where $G = 2\pi/P_s$ denotes the reciprocal lattice vector of the SPPs coupler, where three meta-atoms form a super cell with a period of $P_s = 0.87\lambda \approx 930$ nm. According to the argument presented in Section 2.1, we understand that our meta-coupler should be designed to exhibit a phase gradient $\zeta = 2\pi/0.87\lambda = k_{\text{SPP}}$.

Guided by the design principle described in Section 2.1, we set the orientation angles of all three meta-atoms as $\theta(x) = \pi/4$ and then arrange them sequentially with a distance $P = 310$ nm to form our meta-coupler. Figure 3b depicts the SEM image of our fabricated sample containing both the meta-coupler and the plasmonic metal. According to Equation (2), we find that now all meta-atoms exhibit the desired capability to convert incident LCP

to linear polarization along the x direction, and the whole meta-coupler exhibits the following phase profile

$$\varphi^+(x, y) = \text{const.} - \zeta x, \quad (3)$$

under the illumination of normally incident light with LCP. Here, the phase gradient is $\zeta = 2\pi/P_s$ which is very close to k_{SPP} . Therefore, we expect that our meta-coupler can efficiently convert normally incident LCP light to eigen SPP flowing on the plasmonic metal at the left-hand side, since the driven SW generated on the metasurface exhibits a polarization and \mathbf{k} vector matching those of the eigen SPP. Meanwhile, switching the incident polarization to RCP, Equation (2) tells us that waves reflected by all meta-atoms have the linear polarization along the y -axis, while the phase profile of the metasurface becomes $\varphi^-(x, y) = \zeta_0 - \zeta x - \pi/2$. Interestingly, now the driven SW exhibits a polarization and \mathbf{k} wave vector mismatching with those of the eigen SPP, and thus no SPP wave can be excited.

We experimentally verify the above predictions. Shine the meta-coupler by a Gaussian beam (spot size: $w_0 \approx 8 \mu\text{m}$) exhibiting LCP or RCP, respectively, we employ a LRM system to measure the SPP pattern generated on the device, with detailed experimental setup shown in Figure S3 (Supporting Information).

Figure 3c,d depicts the LRM-recorded images as the meta-coupler is illuminated by normally incident light with LCP and RCP at $\lambda = 1064$ nm, respectively. Clearly, measured results indicate that unidirectional SPP signals are excited on the plasmonic metal in the LCP-incidence case, while no SPP signal exists in the RCP-incidence case, in consistency with our theoretical predictions. We note that certain standing-wave component exists in the pattern shown in Figure 3c, which is caused by the interference between incident SPP and partially reflected SPP on the sample boundary.

We further analyze the LRM image in Figure 3c to evaluate the SPP propagation length L_p , the coupling efficiency, as well as the utilization efficiency (the ratio between power carried by SPP flowing to the left direction and that of the total SPP generated) of the device. Red circles in Figure 3e represent how $I_x x$ (with I_x being the LRM intensity measured at x) varies against x . Fitting the measured $I_x x \sim x$ curve with the formula $\ln(I_x x) = \ln(S) - x/L_p$ (see black solid line) where S is a constant, we obtain that $L_p \approx 26$ μm . Using the method described in refs. [6] and [48] to evaluate the coupling efficiency and the SPP utilization efficiency based on our experimental data, we find that they are 35% and 98%, respectively. We also performed FDTD simulations to evaluate these two efficiencies, and found that they are 60% and 99%, respectively. We note that the experimental coupling efficiency is lower than the simulated one, which can be attributed to sample imperfections, nonideal excitation and additional losses contributed by boundary scatterings. While the demonstrated efficiencies are already high in this frequency regime, they are not close to 100% due to relatively large absorption loss of Au and scattering losses caused by impedance mismatch in this side-coupling configuration.^[5,35,49] The efficiency can be further improved by choosing low-loss materials (e.g., Ag or dielectrics) and adopting new coupling configuration.^[7] Nevertheless, both the coupling efficiency and the SPP utilization efficiency of our meta-coupler are substantially higher than those of the grating coupler, which are 10% and 50% (see Figure S4, Supporting Information), respectively.

2.3. An Arc-Shaped Coupler: Excitation and Focusing of SPP

Encouraged by the above benchmark tests on the stripe-shape SPP coupler, we proceed to demonstrate the excitation and focusing of SPP based on an arc-shape meta-coupler. Figure 4a schematically shows the designed meta-coupler in a shape of quarter ring belt. Guided by the design principle described in Section 2.1, we set the orientation angles of all three meta-atoms as $\theta(r, \phi) = \pi/4 + \phi$, so that each meta-atom can convert incident LCP to LP orientated along the radial direction [see Equation (2)]. We further place meta-atoms of different types in a C-B-A sequence along the radial direction. Put all this information into Equation (2), we find that the whole meta-device under the LCP incidence exhibits a phase profile

$$\varphi^+(r, \phi) = \text{const.} + \phi - \zeta r, \quad (4)$$

with $\zeta = 2\pi/P_s \approx k_{\text{spp}}$ being the desired phase gradient and ϕ is restricted in the range of $[-\frac{\pi}{4}, \frac{\pi}{4}]$. Therefore, under the excitation of LCP light, the driven SW generated by the meta-coupler exhibits both *correct* local polarization and **k** vector matching those

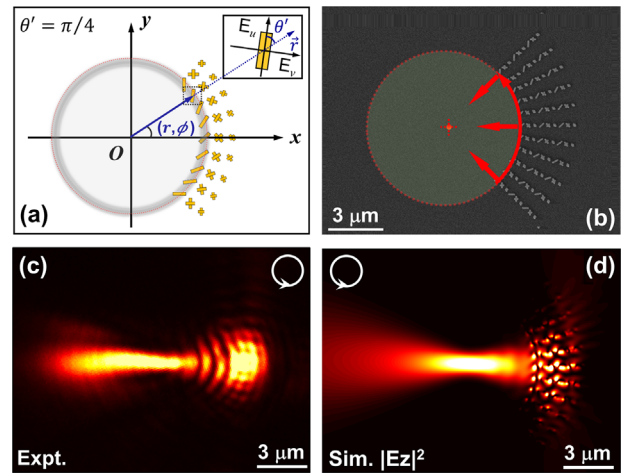


Figure 4. Design and characterization of the arc-shaped SPP coupler. a) Schematic diagram of the designed arc-shaped SPP coupler. b) SEM image of the fabricated sample. c) LRM-measured and d) FDTD-simulated E-field intensity distributions on the sample as the coupler is shined by normally incident light at 1064 nm with LCP.

of the cylindrically polarized eigen SPP supported by the plasmonic metal. We thus expect that such a device can efficiently excite a cylindrically polarized SPP flowing to the origin of the ring, resulting in SPP focusing as desired.

We fabricate out the designed meta-coupler (see Figure 4b for its SEM image) and experimentally characterize its performance. Figure 4c,d depicts, respectively, measured and FDTD-simulated E-field intensity distribution of the excited SPPs as the meta-coupler is illuminated by normally incident LCP light at 1064 nm. Clearly, FDTD simulations are in nice agreement with measured results, both showing that our meta-device can excite SPP with high efficiency and then focus the generated SPP into the origin point, where the intensity distribution of E_z component is applied to compare with the measured result since E_z is the dominant field component inside the SPP wave. For the focused SPP waves, partially reflected SPP by the sample boundary cannot spatially overlap with the incident ones, and thus no standing wave patterns can be formed in Figure 4c.

2.4. A High-Efficiency Vector and Vortex Plasmonic Lens

We now realize the final device and experimentally demonstrate that it can generate vector SPP vortices with a high efficiency. As schematically shown in Figure 5a, our device is a ring-belt-shape coupler composed of three meta-atoms designed in Section 2.1. Following the design principle discussed in Section 2.1, we set the orientation angles of all meta-atoms as $\theta(r, \phi) = \pi/4 + \phi$ and arrange three different meta-atoms in a sequence C-B-A along the radial direction. According to Equation (2), we find that our device exhibits a profile

$$\varphi^+(r, \phi) = \text{const.} + \phi - \zeta r, \quad (5)$$

under the LCP incidence. We note that Equation (5) is essentially the same as Equation (4), only with now ϕ varying in the whole range of $[-\pi, \pi]$. Extending the variation range of ϕ to 2π is

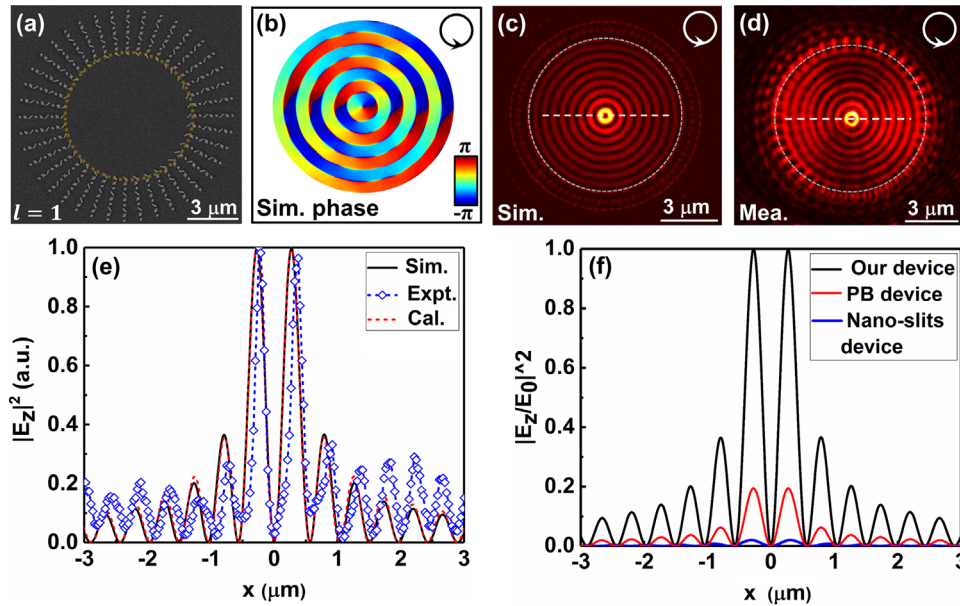


Figure 5. Characterization of our high-efficiency vector and vortex plasmon lens. a) SEM image of the fabricated sample. b) FDTD-simulated optical phase distribution of the E_z field in the focusing region as our meta-coupler is shined by normally incident LCP light at $\lambda = 1064$ nm. c,d) FDTD-simulated $|E_z|^2$ and measured E-field intensity distributions on the sample as the coupler is shined by normally incident light at 1064 nm with LCP. e) Distributions of $|E_z|^2$ along the central symmetric line [the white dashed line passing the origin in (c) and (d)], retrieved from the simulated pattern (black solid curve) and the measured pattern (blue symbols), and obtained by analytical calculations (red dotted curve). f) FDTD-computed $|E_z/E_0|^2$ distributions with E_0 as a constant along the central symmetrical line in three different systems containing the present meta-coupler (black solid curve), the PB meta-coupler (red solid curve), and the nanoslit-based meta-coupler (blue solid curve), respectively, as the meta-couplers are shined by the same normally incident light with LCP. The configurations of the PB meta-coupler and the nanoslit-based meta-coupler are shown in Figure S8 (Supporting Information).

important, since the phase gradient term ϕ along the azimuthal direction in Equation (5) can now contribute an orbital angular momentum (OAM) with a topological charge $l = 1$ to the generated SPP, as we demonstrate in the following.

We perform both experiments and simulations to characterize the SPP pattern generated by our meta-device. Figure 5b shows the simulated optical phase distribution of the E_z field in the focusing region as our meta-coupler is shined by normally incident LCP light at $\lambda = 1064$ nm. A 2π phase variation along tangential direction can be observed in Figure 5b, which is consistent with our theoretical prediction of forming an SPP vortex carrying an OAM with $l = 1$. Figure 5c,d illustrates the simulated and measured distributions of E-field generated on the device surface, as the meta-coupler is illuminated by normally incident LCP light. Experimental results are in good agreement with simulations. We find two clear features from the obtained patterns. First, a dark spot exists in the center of the inner region, which is the clear feature of the vortex generation. Second, strength of generated electric field generally decays as leaving the origin accompanying with oscillations with a period of $\lambda_{\text{SPP}}/2$, which is a clear manifestation of SPP interference. These features are more clearly illustrated in Figure 5e where the measured (symbols) and simulated (solid line) E-field distributions along the line passing the origin (dashed lines in Figure 5c,d) are compared. Nice agreement is noted between measured and simulated patterns. The oscillation period w is found as $w \approx 0.46$ μm in experiment and $w \approx 0.4635$ μm in simulation, both being very close to $\frac{\lambda_{\text{SPP}}}{2} = 0.465$ μm . Moreover, to further reveal the spiral properties of the vortex SPP, we also measured the interference fringes of

the leakage vortex SPP with a spherical wave and a plane wave, as shown in Figure S5a,b (Supporting Information), respectively.

We establish an analytical model to understand the physics behind the discovered effect. We first examine the SPP wave generated by a single array of meta-atoms located at the line with angle $\phi' = 0^\circ$, under the illumination of normally incident LCP light at 1064 nm. Treating such a line-coupler under excitation as a dipole source, we find from Green's function calculations that the generated SPP wave can be described as $E_z(\mathbf{r}) = \eta H_0^{(1)}(k_{\text{SPP}}|\mathbf{r} - \mathbf{r}'|)$ where \mathbf{r}' denotes the position of the dipole and η is a constant proportional to the coupling efficiency. Such a formula is well justified by comparing the field distributions along the radial line at $\phi = 0^\circ$ obtained by FDTD simulation and the analytical formula (see Figure S6 and other detailed comparisons in Supporting Information). For another line-coupler located at a different angle ϕ' , it is straightforward to derive that the SPP wave generated by it (under LCP excitation) can be written as $E_z'(\mathbf{r}) = \eta H_0^{(1)}(k_{\text{SPP}}|\mathbf{r} - \mathbf{r}'|) e^{i\phi'}$, since the only difference between SPP waves generated by line-couplers at different angles is the phase factor of $e^{i\phi'}$. Therefore, the total SPP wave generated by the whole coupler can be obtained by

$$E_z(r, \phi) = \eta \int_0^{2\pi} H_0^{(1)}(k_{\text{SPP}}|r - r'|) e^{i\phi'} \cdot \frac{d\phi'}{2\pi} = C\eta J_1(k_{\text{SPP}}r) e^{i\phi} \quad (6)$$

where C is a constant. We use Equation (6) to calculate the E-field distribution along the dashed line in Figure S7 (Supporting

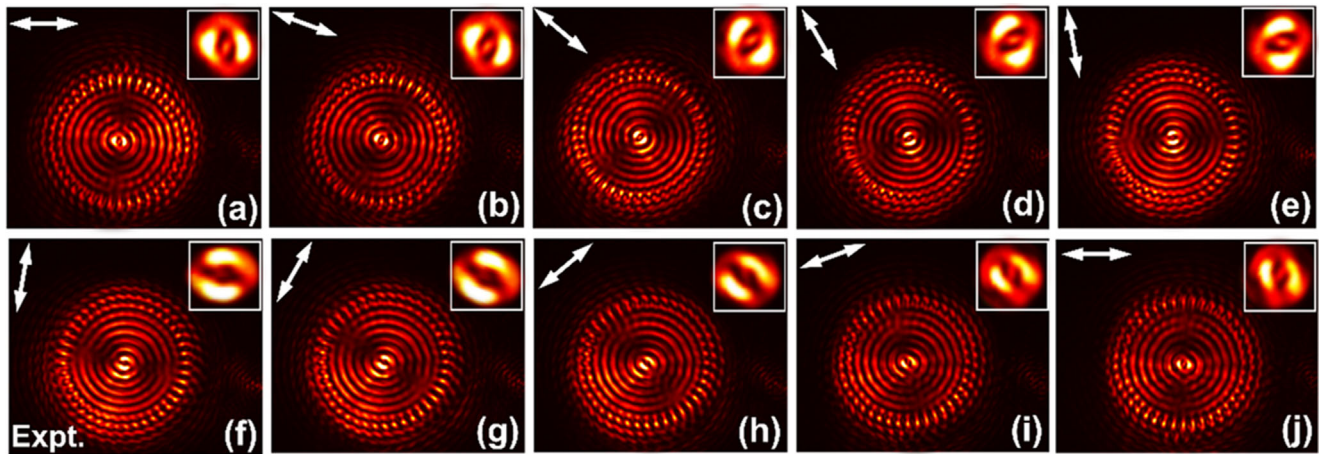


Figure 6. LRM-recorded SPP patterns on the device surface, with a polarizer placed in front of the detector and rotated along (a) 0°, (b) 20°, (c) 40°, (d) 60°, (e) 80°, (f) 100°, (g) 120°, (h) 140°, (i) 160° and (j) 180° (see white double-head arrows).

Information), and depict the results in Figure 5e as a red dashed line. As it is difficult to compare the absolute values of E-fields obtained by different approaches, we normalize all these patterns in such a way that the peak values in these patterns are set as 1. The analytically calculated field distribution is in excellent agreement with the FDTD-simulated one. Analytical formula (6) can help us understand many intriguing features discovered experimentally and numerically. First, the generated SPP standing-wave pattern carries an OAM with a topological charge $l = 1$ due to the factor $e^{i\phi}$ [see Figure S7, Supporting Information, for the distributions of E-field intensity and optical phase computed by Equation (6)]. Second, the intensity oscillation period along the radial direction is $w = \pi/k_{\text{spp}}$ since the function $|J_1(k_{\text{spp}}r)|$ exhibits zeros at the positions satisfying $k_{\text{spp}}r = m\pi$. Finally, the peak value of the near-field generated in the center is proportional to the coupling efficiency η of the device.

We compare the performance of our meta-device with those of two other meta-devices previously studied. We design two ring-belt meta-couplers exhibiting the same sizes as our device, only with unit cells replaced by nanoslits or PB meta-atoms possessing 100% PCR. We then employ FDTD simulations to compute the SPP standing-wave patterns generated in two cases (see Figure S8, Supporting Information), as two meta-couplers are shined by the same LCP light as in the case of Figure 5b,c. FDTD simulated E-field distributions along the central dashed line in three cases are compared in Figure 5f, where the SPP intensity are normalized by the peak value E_0 of our device. While these three curves exhibit similar overall shapes, the maximum local-field generated by our meta-coupler is five times higher than that by the PB meta-coupler and is 50 times higher than that by the nanoslit-based meta-coupler. The ratios between these values precisely reflect the differences in coupling efficiencies and utilization efficiencies of these meta-couplers.

Finally, we characterize the polarization distribution of the generated SPP vortex. Figure 6a–j shows the measured intensity profiles of the generated SPP vortex recorded by our LRM with a polarizer tilted at different angles (denoted by white arrows) placed in front of the detector, while the corresponding FDTD-simulated patterns are depicted in Figure S9 (Supporting Infor-

mation) for comparison. Insets in subfigures show the zoomed-in pictures of the central area in different cases. These polarization angle-dependent patterns clearly illustrate that the generated SPP patterns are cylindrically polarized.

3. Conclusions and Perspectives

In summary, we established a generic approach to generate pre-designed near-field SPP patterns with high efficiencies. Composed by a series of meta-atoms which possess both desired reflection phases and polarization-conversion capabilities, our meta-devices can efficiently convert CP light to SPP waves with desired wave-fronts and polarization distributions. After two benchmark experiments based on meta-devices in stripe and arc shapes, we experimentally demonstrated the generation of a vector SPP vortex with a topological charge $l = 1$, with intensity much higher than those realized by previous meta-couplers. All experimental results are in excellent agreement with FDTD simulations and analytical calculations, revealing the crucial role played by our meta-atoms exhibiting much higher SPP coupling efficiencies.

Overall, our work establishes an efficient, generic, and flexible platform for generating pre-designed near-field patterns, which are useful in both fundamental researches and photonic applications. Other vector SPP standing-wave patterns can also be realized based on specifically designed meta-couplers. For example, we show in supporting information that vector SPP vortices with different topological charges can be realized through constructing meta-couplers with meta-atoms arranged in different ways (see Figure S10, Supporting Information). Experimentally realizing these special near-field patterns with much enhanced local fields and applying them to boosting light-matter interactions are interesting and challenging future projects.

4. Experimental Section

Numerical Simulations: Full-wave simulations were performed using the software FDTD solution. In the simulations, permittivity of Au was described by the Drude model $\epsilon_r(\omega) = \epsilon_\infty - \omega_p^2/(\omega(\omega + i\gamma))$, where $\epsilon_\infty = 9$,

$\omega_p = 1.367 \times 10^{16} \text{ s}^{-1}$, and $\gamma = 1.224 \times 10^{14} \text{ s}^{-1}$ obtained by fitting with experiment results. The SiO_2 spacer was considered as a lossless dielectric slab with permittivity $\epsilon = 2.08$, and the dielectric loss was effectively considered in choosing appropriate damping parameter for Au through fitting with experimental data. For simulations on reflection properties of meta-atoms, periodic boundary conditions were applied on the simulation boundaries. For simulations on finite structures, absorbing boundary conditions were implemented on the boundaries to remove the energy flowing outside the simulation domain and the energy bounced at the boundary.

Sample Fabrications: All MIM tri-layer samples were fabricated using standard thin-film deposition and electron-beam lithography (EBL) techniques. First, 5 nm Cr, 150 nm Au, 5 nm Cr, and 180 nm SiO_2 dielectric layer were sequentially deposited on the surface of a silicon substrate using magnetron DC sputtering (Cr and Au) and RF sputtering (SiO_2). Second, the cross nanostructures were lithographed with EBL on an ≈ 100 nm thick PMMA2 layer at an acceleration voltage of 20 keV. After development in a solution of methyl isobutyl ketone and isopropyl alcohol, a 5 nm Cr adhesion layer and a 30 nm Au layer were subsequently deposited using thermal evaporation. The Au patterns were finally formed on top of the SiO_2 film after a lift-off process using acetone.

Supporting Information

Supporting Information is available from the Wiley Online Library or from the author.

Acknowledgements

F.L. and D.W. contributed equally to this work. This work was supported by the National Key Research and Development Program of China (Nos. 2022YFA1404701 and 2020YFA0710100), the National Natural Science Foundation of China (Nos. 12221004, 11734007, 62192771, 62005197, and 11874118), and the Natural Science Foundation of Shanghai (No. 20JC1414601). The authors acknowledge the technical support from the Fudan Nanofabrication Laboratory for sample fabrication.

Conflict of Interest

The authors declare no conflict of interest.

Data Availability Statement

The data that support the findings of this study are available from the corresponding author upon reasonable request.

Keywords

radial polarization, surface plasmon polaritons, vector & vortex plasmon lens, vortex wavefront

Received: December 20, 2022

Revised: February 28, 2023

Published online: March 25, 2023

[1] W. L. Barnes, A. Dereux, T. W. Ebbesen, *Nature* **2003**, 424, 6950.

[2] E. Ozbay, *Science* **2006**, 311, 5758.

[3] M. A. Seo, H. R. Park, S. M. Koo, D. J. Park, J. H. Kang, O. K. Suwal, S. S. Choi, P. C. M. Planken, G. S. Park, N. K. Park, Q. H. Park, D. S. Kim, *Nat. Photonics* **2009**, 3, 3.

- [4] F. J. Garcia-Vidal, A. I. Fernandez-Dominguez, L. Martin-Moreno, H. C. Zhang, W. X. Tang, R. W. Peng, T. J. Cui, *Rev. Mod. Phys.* **2022**, 94, 2.
- [5] S. L. Sun, Q. He, S. Y. Xiao, Q. Xu, X. Li, L. Zhou, *Nat. Mater.* **2012**, 11, 5.
- [6] A. Pors, M. G. Nielsen, T. Bernardin, J. C. Weeber, S. I. Bozhevolnyi, *Light: Sci. Appl.* **2014**, 3, 197.
- [7] W. J. Sun, Q. He, S. L. Sun, L. Zhou, *Light: Sci. Appl.* **2016**, 5, 3.
- [8] H. Wei, D. Pan, S. P. Zhang, Z. P. Li, Q. Li, N. Liu, W. H. Wang, H. X. Xu, *Chem. Rev.* **2018**, 118, 6.
- [9] Z. Y. Fang, L. R. Fan, C. F. Lin, D. Zhang, A. J. Meixner, X. Zhu, *Nano Lett.* **2011**, 11, 4.
- [10] Y. Zhang, Y. H. Xu, C. X. Tian, Q. Xu, X. Q. Zhang, Y. F. Li, X. X. Zhang, J. G. Han, W. L. Zhang, *Photonics Res.* **2018**, 6, 18.
- [11] L. L. Yin, V. K. Vlasko-Vlasov, J. Pearson, J. M. Hiller, J. Hua, U. Welp, D. E. Brown, C. W. Kimball, *Nano Lett.* **2005**, 5, 7.
- [12] W. Nomura, M. Ohtsu, T. Yatsui, *Appl. Phys. Lett.* **2005**, 86, 18.
- [13] N. Fang, H. Lee, C. Sun, X. Zhang, *Science* **2005**, 308, 5721.
- [14] I. I. Smolyaninov, Y. J. Hung, C. C. Davis, *Science* **2007**, 315, 5819.
- [15] R. Dorn, S. Quabis, G. Leuchs, *Phys. Rev. Lett.* **2003**, 91, 23.
- [16] X. Hao, C. F. Kuang, T. T. Wang, X. Liu, *Opt. Lett.* **2010**, 35, 23.
- [17] K. T. Gahagan, G. A. Swartzlander, *J. Opt. Soc. Am. B* **1999**, 16, 4.
- [18] M. E. J. Friese, T. A. Nieminen, N. R. Heckenberg, H. Rubinsztein-Dunlop, *Nature* **1998**, 394, 6702.
- [19] T. Bauer, S. Orlov, U. Peschel, P. Banzer, G. Leuchs, *Nat. Photonics* **2014**, 8, 23.
- [20] J. Scheuer, M. Orenstein, *Science* **1999**, 285, 5425.
- [21] S. Y. Lee, S. J. Kim, H. Kwon, B. Lee, *IEEE Photonics Technol. Lett.* **2015**, 27, 7.
- [22] C. T. Ku, H. N. Lin, C. B. Huang, *Appl. Phys. Lett.* **2015**, 106, 5.
- [23] C. D. Ku, W. L. Huang, J. S. Huang, C. B. Huang, *IEEE Photonics J.* **2013**, 5, 3.
- [24] Y. Gorodetski, A. Niv, V. Kleiner, E. Hasman, *Phys. Rev. Lett.* **2008**, 101, 4.
- [25] H. Kim, J. Park, S. W. Cho, S. Y. Lee, M. Kang, B. Lee, *Nano Lett.* **2010**, 10, 2.
- [26] C. F. Chen, C. T. Ku, Y. H. Tai, P. K. Wei, H. N. Lin, C. B. Huang, *Nano Lett.* **2015**, 15, 4.
- [27] Y. Zhang, R. R. Zhang, X. Li, L. Ma, C. X. Liu, C. W. He, C. F. Cheng, *Opt. Express* **2017**, 25, 25.
- [28] Y. Q. Zhang, X. Y. Zeng, L. Ma, R. R. Zhang, Z. J. Zhan, C. Chen, X. R. Ren, C. W. He, C. X. Liu, C. F. Cheng, *Adv. Opt. Mater.* **2019**, 7, 18.
- [29] Y. H. Guo, M. B. Pu, F. Zhang, M. F. Xu, X. L. Ma, X. G. Luo, *Photonics Insight* **2022**, 1, R03-1.
- [30] W. Y. Tsai, J. S. Huang, C. B. Huang, *Nano Lett.* **2014**, 14, 2.
- [31] A. Liu, G. Rui, X. Ren, Q. Zhan, G. Guo, G. Guo, *Opt. Express* **2012**, 20, 22.
- [32] M. L. Juan, M. Righini, R. Quidant, *Nat. Photonics* **2011**, 5, 6.
- [33] A. Pors, M. G. Nielsen, R. L. Eriksen, S. I. Bozhevolnyi, *Nano Lett.* **2013**, 13, 2.
- [34] W. T. Chen, K. Y. Yang, C. M. Wang, Y. W. Huang, G. Sun, I. D. Chiang, C. Y. Liao, W. L. Hsu, H. T. Lin, S. L. Sun, L. Zhou, A. Q. Liu, D. P. Tsai, *Nano Lett.* **2014**, 14, 1.
- [35] Z. Wang, S. Q. Li, X. Q. Zhang, X. Feng, Q. W. Wang, J. G. Han, Q. He, W. L. Zhang, S. L. Sun, L. Zhou, *Adv. Sci.* **2020**, 7, 19.
- [36] S. L. Sun, K. Y. Yang, C. M. Wang, T. K. Juan, W. T. Chen, C. Y. Liao, Q. He, S. Y. Xiao, W. T. Kung, G. Y. Guo, L. Zhou, D. P. Tsai, *Nano Lett.* **2012**, 12, 12.
- [37] N. F. Yu, P. Genevet, M. A. Kats, F. Aieta, J. P. Tetienne, F. Capasso, Z. Gaburro, *Science* **2011**, 334, 6054.
- [38] X. Y. Zhang, Q. Li, F. F. Liu, M. Qiu, S. L. Sun, Q. He, L. Zhou, *Light: Sci. Appl.* **2022**, 9, 3.

- [39] Y. Fan, B. Cluzel, M. Petit, X. Le Roux, A. Lupu, A. de Lustrac, *ACS Appl. Mater. Interfaces* **2020**, *12*, 18.
- [40] J. M. Hao, Y. Yuan, L. X. Ran, T. Jiang, J. A. Kong, C. T. Chan, L. Zhou, *Phys. Rev. Lett.* **2007**, *99*, 6.
- [41] W. J. Sun, Q. He, J. M. Hao, L. Zhou, *Opt. Lett.* **2011**, *36*, 6.
- [42] V. Parigi, V. D'Ambrosio, C. Arnold, L. Marrucci, F. Sciarrino, J. Laurat, *Nat. Commun.* **2015**, *6*, 7706.
- [43] F. Y. Yue, D. D. Wen, J. T. Xin, B. D. Gerardot, J. S. Li, X. Z. Chen, *ACS Photonics* **2016**, *3*, 9.
- [44] Z. Bomzon, G. Biener, V. Kleiner, E. Hasman, *Opt. Lett.* **2002**, *27*, 13.
- [45] N. Shitrit, I. Bretner, Y. Gorodetski, V. Kleiner, E. Hasman, *Nano Lett.* **2011**, *11*, 5.
- [46] W. J. Luo, S. Y. Xiao, Q. He, S. L. Sun, L. Zhou, *Adv. Opt. Mater.* **2015**, *3*, 8.
- [47] J. W. Duan, H. J. Guo, S. H. Dong, T. Cai, W. J. Luo, Z. Z. Liang, Q. He, L. Zhou, S. L. Sun, *Sci. Rep.* **2017**, *7*, 1354.
- [48] D. Y. Wang, F. F. Liu, T. Liu, S. L. Sun, Q. He, L. Zhou, *Light: Sci. Appl.* **2021**, *10*, 67.
- [49] C. Qu, S. Y. Xiao, S. L. Sun, Q. He, L. Zhou, *Europhys. Lett.* **2013**, *101*, 5.